# Matrix-Construction Calibration Method for Antenna Arrays

**ERIC K. L. HUNG**
Defence Research Establishment Ottawa

**The experimental evaluation of a calibration method [1] developed for receive antenna arrays is presented. The method constructs a calibration matrix to compensate for unequal gain and phase responses at the array elements, mutual coupling among the elements, and small errors in element positions. The results showed that the method 1) reduced the deviation of the element gain patterns from the isolated-element patterns, the deviation of array beam patterns from the ideal patterns, the errors in relative element output powers and phases, and the errors in direction estimates using single-target and two-target array snapshots; 2) increased the alignment of single-target array snapshots with array steering vectors and the probability of resolving two targets as their angular separation decreased to zero; 3) produced essentially the same calibration matrix with different sets of calibration data; and 4) was highly tolerant to unknown interference in the calibration data.**

Manuscript received June 25, 1998; revised November 26, 1999 and January 26, 2000; released for publication February 2, 2000.

IEEE Log No. T-AES/36/3/07800.

Refereeing of this contribution handled by K. J. Sangston.

Author's address: Surface Radar Section, Defence Research Establishment Ottawa, 3701 Carling Avenue, Ottawa, Ontario, Canada K1A 0K2.



0018-9251/00/$10.00 2000 IEEE

## I. INTRODUCTION

Antenna arrays are usually used in conjunction with high-resolution direction-finding methods such as the multiple signal classification (MUSIC) [2] and forward-backward Kumaresan-Tufts singular value decomposition (TKSVD) [3, 4] methods to detect targets and resolve their directions. These arrays must be accurately calibrated, because a perfectly calibrated array has the lowest signal-to-noise ratio requirement for target detection and produces the most accurate estimates of target directions. Some studies on the effect of calibration errors on direction estimates are given in [5–9].

The most accurate method to calibrate an antenna array is to move a pilot source over a fine grid of directions covered by the array and measure the array response vectors (array manifold vectors) for these directions. However, the method is impractical, because the computational load in direction-finding with these vectors is extremely high. Besides, when multipath interference is unavoidable in the calibration experiment, a new set of array response vectors may have to be generated periodically to account for changes in local conditions (e.g., a change from a wet spring to a dry autumn).

The alternative methods treat antenna calibration as a parameter estimation problem. They note that the outputs of the array elements are usually corrupted by one or more error sources such as unequal gain and phase responses at the element sensors, mismatches in cables and receiver electronics at the elements, mutual coupling among the elements, and small errors in element positions. Each method calculates a set of calibration coefficients for the array and uses it to suppress the targeted errors at the outputs of the elements.

Several parametric methods have been developed to suppress all of the above errors in narrowband arrays. They include the auto-calibration method of Weiss and Friedlander [10] and the calibrate-only methods of Pierre and Kaveh [11], See [12], and Hung [1]. These methods assume that the effects of the error sources can be represented by a matrix operation. They are different. The method in [10] does not always have unique solutions. The reasons are given in [11] for linear arrays and in [13] for nonlinear arrays. The method in [11] equates the complex signal amplitudes in every array snapshot to unity. This restricts the application of the method. The methods in [12 and 1] are derived from the one in [11] by including the computation of signal amplitudes in the snapshots. They differ in that the method in [12] is designed for white noise interference only, while the method in [1] also includes some tolerance to unknown interference. This tolerance was not mentioned or illustrated in [1].

An evaluation of the method in [1] with experimental data is presented here. It is designed to illustrate that the method 1) improves the array characteristics and the accuracy of direction estimates obtained from the array snapshots; 2) produces essentially the same calibration matrix with different sets of calibration data, if each set satisfies all the measurement conditions of the calibration method; and 3) is highly tolerant to unknown interference.

The evaluation is comprehensive, because a thorough evaluation of an antenna array calibration method has not yet been published in the open literature. It can distinguish methods that improve the array performances for all signal directions from those that optimize the performances for some directions only. It can also distinguish methods that can calibrate antenna arrays under harsh interference conditions from those that require controlled environments.

In the following, Section II contains a brief description of the calibration method. Section III discusses the experimental data and the calibration matrix they produce. Section IV provides an evaluation of the calibration method, and Section V presents the conclusions.

## II. CALIBRATION METHOD

A brief description of the calibration method in [1] is presented here. It includes the signal model used, the assumptions made, and the computational procedure.

### A. Signal Model

The array has $N$ elements. A pilot source is present. An ideal array snapshot for source direction $\theta_m$ is given by

$$\mathbf{x}_m = \alpha_m \mathbf{a}_m \tag{1}$$

where $\alpha_m$ is the complex signal amplitude in $\mathbf{x}_m$, and $\mathbf{a}_m$ is the array steering vector for direction $\theta_m$. This expression assumes a perfectly calibrated array, a pure tone signal, no interaction among the array elements, no noise, and no interference.

The corresponding measured array snapshot is given by $\mathbf{y}_m$, with

$$\mathbf{y}_m = \mathbf{B}\mathbf{x}_m + \mathbf{e}_m. \tag{2}$$

Matrix $\mathbf{B}$ is $N \times N$. It depends on relative element gain and phase responses at the element sensors, mismatches in cables and receiver electronics, mutual coupling among the array elements, and errors in sensor locations. Vector $\mathbf{e}_m$ denotes the sum of interference and noise.

Let $\{\mathbf{y}_1, \mathbf{y}_2, \ldots, \mathbf{y}_M\}$ be a set of $M$ array snapshots measured with source directions $\{\theta_1, \theta_2, \ldots, \theta_M\}$, respectively. The calibration matrix calculated with this set is identified here as the $N \times N$ matrix $\mathbf{C}$ that, together with the estimates of $\{\alpha_1, \alpha_2, \ldots, \alpha_M\}$, minimizes the objective function

$$S = \sum_{m=1}^{M} |\mathbf{C}\mathbf{y}_m - \hat{\mathbf{x}}_m|^2 \tag{3}$$

subject to the uniqueness condition

$$C_{11} = 1.0. \tag{4}$$

Vector $\hat{\mathbf{x}}_m$ will be calculated as the component of $\mathbf{C}\mathbf{y}_m$ in the direction of $\mathbf{a}_m$. The $\hat{}$ denotes the estimate and $C_{pq}$ denotes the $pq$th coefficient of $\mathbf{C}$.

The function $S$ depends on the signal amplitude estimates $\hat{\alpha}_1$ to $\hat{\alpha}_M$ in $\hat{\mathbf{x}}_1$ to $\hat{\mathbf{x}}_M$, respectively. Matrix $\mathbf{C}^{-1}$ is proportional to $\mathbf{B}$ in the special case of zero noise and interference, so that each $\mathbf{e}_m$ is a null vector.

In later discussions, the superscripts T and H denote the transpose and conjugate-transpose, respectively; the set $\{a_{1m}, a_{2m}, \ldots, a_{Nm}\}$, for example, denotes the $N$ components of $\mathbf{a}_m$, and $\mathbf{y}_m^c$, defined as

$$\mathbf{y}_m^c = \mathbf{C}\mathbf{y}_m \tag{5}$$

denotes the calibrated snapshot calculated with $\mathbf{y}_m$. To avoid confusions on directions, $a_{nm}$ and $\mathbf{a}_m$ are sometimes denoted by $a_n(\theta_m)$ and $\mathbf{a}(\theta_m)$, respectively.

### B. Measurement Conditions

The following conditions are assumed to be satisfied.

1) The array elements are narrowband.
2) The process that converts an ideal snapshot to a measured snapshot can be approximated by a matrix operation.
3) The calibration data are generated by moving a single pilot source over the range of directions covered by the array in normal operations.
4) The number of array snapshots in the calibration data is sufficiently large.
5) A preliminary calibration has been carried out, so that one can obtain rough estimates of the complex signal amplitudes from the array snapshots.

Conditions 3 and 4 are needed for tolerance to unknown interference, including diffuse and specular multipath. Together, they attempt to destroy the correlation between the pilot signal and any interference by effectively randomizing their phase difference in the data. They also cause each fixed-direction interference source to behave like spatially distributed interference by forcing the angular separation between it and the pilot signal to spread over a wide range of values.

The number of snapshots required in condition 4 is the number required for $\mathbf{C}$ to reach the asymptotic limit as this number increases. A method to check if condition 4 is satisfied is given at the end of Section III.

### C. Computation of Calibration Matrix

The calculation of $\mathbf{C}$ is based on the following observations.

1) If $\mathbf{C}_{i-1}$ is an estimate of $\mathbf{C}$ and

$$\mathbf{z}_m = \mathbf{C}_{i-1}\mathbf{y}_m \tag{6}$$

a least square estimate of the $\alpha_m$ in (1) is

$$\hat{\alpha}_m = \mathbf{a}_m^H \mathbf{z}_m / |\mathbf{a}_m|^2 \tag{7}$$

and an estimate of $\mathbf{x}_m$ is

$$\hat{\mathbf{x}}_m = \hat{\alpha}_m \mathbf{a}_m. \tag{8}$$

2) Given the $N \times M$ matrices $\hat{\mathbf{X}}$ and $\mathbf{Y}$, where $\hat{\mathbf{X}} = (\hat{\mathbf{x}}_1, \hat{\mathbf{x}}_2, \ldots, \hat{\mathbf{x}}_M)$ and $\mathbf{Y} = (\mathbf{y}_1, \mathbf{y}_2, \ldots, \mathbf{y}_M)$, one can get a new estimate of $\mathbf{C}$ by solving the equation

$$\mathbf{C}_i \mathbf{Y} = \hat{\mathbf{X}} \tag{9}$$

as

$$\mathbf{C}_i = (\hat{\mathbf{X}}\hat{\mathbf{X}}^{\mathrm{H}})(\mathbf{Y}\hat{\mathbf{X}}^{\mathrm{H}})^{-1} \tag{10}$$

and imposing the uniqueness condition (4) on $\mathbf{C}_i$. The inverse $(\mathbf{Y}\hat{\mathbf{X}}^{\mathrm{H}})^{-1}$ exists, because of measurement conditions 3 and 4.

3) The initialization

$$\mathbf{C}_0 = \mathbf{I}_N \tag{11}$$

where $\mathbf{I}_N$ is an $N \times N$ identity matrix, is equivalent to using the original data in the first iteration, where $i = 1$.

4) Let

$$\mathbf{D}_i = \mathbf{C}_i - \mathbf{C}_{i-1} \tag{12}$$

and

$$\Delta_i = \max\{|D_{pq}| : p,q = 1,2,\ldots,N\}. \tag{13}$$

One can terminate the iteration if 1) $\Delta_i < \Delta'$, where $\Delta'$ is a prespecified small value, or 2) $i = i_{\max}$, where $i_{\max}$ is the maximum number of iterations specified.

There are six steps in the procedure.

*Step* 1 Specify $\Delta'$ and $i_{\max}$.
Let $i = 1$ and $\mathbf{C}_0 = \mathbf{I}_N$.
*Step* 2 Calculate $\{\hat{\mathbf{x}}_1, \hat{\mathbf{x}}_2, \ldots, \hat{\mathbf{x}}_M\}$, using (6) to (8).
*Step* 3 Calculate $\mathbf{C}_i$ with (10).
*Step* 4 Impose uniqueness condition (4) on $\mathbf{C}_i$.
*Step* 5 Calculate $\Delta_i$ with (12) and (13).
*Step* 6 If $\Delta_i < \Delta'$ or $i = i_{\max}$,
Terminate the iterations and identify $\mathbf{C}_i$ as $\mathbf{C}$.
Else,
Replace $i$ by $i + 1$ and return to Step 2.

## III. EXPERIMENTAL DATA AND CALIBRATION MATRIX

This section contains a brief description of the experimental data and the calibration matrix they produced.

TABLE I
Data Files Used to Study Calibration Method

| File | Size $M$ | Azimuth (°) $\theta_1$ | $\theta_M$ |
|---|---|---|---|
| 1 | 3055 | 19 | −60 |
| 2 | 4246 | −55 | 55 |
| 3 | 4255 | 55 | −55 |

*Note*: File size $M$ is number of array snapshots. Angles $\theta_1$ and $\theta_M$ are source directions in first and $M$th snapshots, respectively.

### A. Experimental Data

The antenna operated at 10 GHz and was a prototype uniform linear array with eight elements ($N = 8$) spaced at a distance of 1.524 cm, or 0.508 wavelength. The sensor in each element was an H-plane sectorial horn rotated 90° about a horizontal axis perpendicular to the front. After rotation, the horn azimuth and elevation beamwidths were 112° and 13.4°, respectively, and the array azimuth beamwidth was 12.5° in the broadside direction. A preliminary study showed that the level of mutual coupling between adjacent horns was −24 to −29 dB.

The calibration data were measured with the horn assembly mounted on a rotating platform and inside a room with fixed pilot sources in the farfield zone of the array. Each horn output was downconverted to an intermediate frequency of 30 MHZ, amplified, passed through synchronous detectors, and sampled with analog-to-digital (A/D) converters. Preprocessing was then carried out to reduce the amplitude of platform vibration in the array snapshots and to remove the snapshots in which the nominal and estimated source directions differed by more than 12.5°. Three files were produced for this study. Their sizes in number of array snapshots, initial source azimuth directions, and final source directions are given in Table I.

The amplitude of platform vibration in snapshot $\mathbf{y}_m$, say, was reduced by replacing the component $y_{nm}$, $n = 1$ to $N$, with $[y_{nm}/a_n(\theta_m + \hat{\varepsilon}_m)]a_n(\theta_m)$. Angle $\theta_m$ was the nominal source direction, $\hat{\varepsilon}_m$ was an estimate of the vibration amplitude, and $a_n(\theta_m + \hat{\varepsilon}_m)$ and $a_n(\theta_m)$ were components of array steering vectors $\mathbf{a}(\theta_m + \hat{\varepsilon}_m)$ and $\mathbf{a}(\theta_m)$, respectively. The set $\{\hat{\varepsilon}_1, \hat{\varepsilon}_2, \ldots, \hat{\varepsilon}_M\}$ was generated by fitting a cosine curve with approximately 20 cycles to the set of error amplitudes $\{\hat{\theta}_1 - \theta_1, \hat{\theta}_2 - \theta_2, \ldots, \hat{\theta}_M - \theta_M\}$, where $\hat{\theta}_m$ was an estimate of the source direction in $\mathbf{y}_m$ and was obtained by matched filtering.

The above procedure reduced many amplitudes of platform vibration from over 2° to less than 0.6°. After the reduction, $\theta_m$ was treated as the true source direction in $\mathbf{y}_m$.

### B. Calibration Matrix

File 2 was used to calculate $\mathbf{C}$, using $i_{\max} = 200$ and $\Delta' = 0.0001$ in Step 1. In the intermediate

TABLE II
Real (Top) and Imaginary (Bottom) Components of Coefficients $\{C_{pq}\}$ in **C**

| | Coefficients in **C** | | | | | | | |
|---|---|---|---|---|---|---|---|---|
| $p$ | $q = 1$ | $q = 2$ | 3 | 4 | 5 | 6 | 7 | 8 |
| 1 | 1.000 | −0.091 | 0.026 | −0.025 | 0.031 | −0.024 | 0.014 | −0.007 |
| | 0.000 | −0.054 | 0.048 | −0.019 | 0.018 | −0.008 | 0.004 | −0.009 |
| 2 | 0.042 | 0.850 | −0.004 | −0.003 | 0.005 | −0.002 | 0.000 | 0.000 |
| | −0.091 | 0.188 | −0.073 | 0.037 | −0.022 | 0.013 | −0.005 | 0.010 |
| 3 | −0.002 | 0.096 | 0.794 | −0.016 | 0.008 | 0.003 | 0.000 | −0.005 |
| | 0.032 | −0.030 | 0.303 | −0.072 | 0.032 | −0.015 | 0.004 | −0.008 |
| 4 | 0.002 | −0.012 | 0.099 | 0.827 | −0.022 | −0.010 | 0.012 | −0.000 |
| | −0.012 | 0.012 | −0.005 | 0.061 | −0.049 | 0.023 | −0.003 | 0.006 |
| 5 | −0.001 | 0.004 | −0.023 | 0.071 | 0.856 | 0.002 | −0.015 | 0.006 |
| | 0.007 | 0.002 | 0.006 | −0.033 | 0.159 | −0.045 | 0.016 | −0.010 |
| 6 | −0.005 | 0.003 | 0.009 | −0.012 | 0.055 | 0.863 | 0.000 | −0.011 |
| | −0.006 | 0.001 | 0.000 | 0.011 | −0.048 | 0.083 | −0.044 | 0.029 |
| 7 | 0.004 | −0.006 | −0.003 | 0.005 | 0.005 | 0.066 | 0.869 | −0.010 |
| | 0.000 | 0.005 | −0.002 | 0.009 | 0.002 | −0.050 | 0.150 | −0.070 |
| 8 | 0.002 | 0.003 | 0.001 | −0.006 | −0.010 | 0.012 | 0.059 | 0.810 |
| | 0.002 | −0.008 | 0.004 | −0.010 | 0.013 | −0.004 | −0.059 | 0.257 |

results, $\Delta_i$ decreased monotonically from 0.338636 to 0.000095 in 108 iterations. The matrix coefficients are given in Table II. They show that **C** is neither diagonal nor symmetric; the coefficients in the main diagonal are different; and, in every row or column, the coefficients generally decrease in magnitude with increasing distance from the diagonal. The inverse $\mathbf{C}^{-1}$ is not presented here. Its properties are similar to those of **C**.

These properties agree with the interpretation that the array elements have unequal gain and phase responses and that there is coupling among the elements.

A verification of measurement condition 4 was made. Here, a new file with 3184 snapshots was constructed by deleting every fourth snapshot from File 2. This new file was used to calculate a new calibration matrix $\mathbf{C}'$ and the difference $\mathbf{C}' - \mathbf{C}$. A study of this difference showed that every coefficient did not exceed 0.002 in magnitude. Because $C'_{11} = C_{11} = 1.0$, it was concluded that **C** was close to the asymptotic limit for infinitely many array snapshots; and that the number of snapshots in File 2 was large enough to satisfy condition 4.

## IV. PERFORMANCE EVALUATION

This evaluation studies the effect of calibration on the element gain patterns, array beam patterns, relative element output powers, errors in relative element output phases, the alignment of single-target array snapshots with array steering vectors, errors in direction estimates, the resolution of two targets, changes in the calibration matrix due to a change in calibration data, and tolerance to interference in the calibration data.

### A. Element Gain Patterns

When mutual coupling is present, the measured element gain patterns usually deviate from those of the isolated elements. There should be a reduction of this deviation after calibration.

File 3 was used to calculate the individual and the average element gain patterns. The gain values in the pattern for the $n$th element, say, were defined as the values in the set $\{|y_{n1}|^2, |y_{n2}|^2, \ldots, |y_{nM}|^2\}$ divided by the largest value. Those of the average pattern were the values in $\{|\mathbf{y}_1|^2, |\mathbf{y}_2|^2, \ldots, |\mathbf{y}_M|^2\}$ divided by the largest value.

The upper half of Fig. 1 shows the individual (dashed lines) and the average (solid) element gain patterns before calibration (B). There are large deviations of individual patterns from the average. In one pattern, the largest value occurs at an azimuth angle of 28° instead of close to 0°. The lower half of Fig. 1 shows the patterns after calibration (A). Here, the deviations are noticeably smaller.

The shapes of the solid lines agree well with measurements, which found that the gain of an isolated element peaked near −7° and that it decreased more slowly from −7° to 80° than from −7° to −80°. From the solid line in the lower half of the figure, an approximate expression for the dependence of relative element output power on $\theta$ is

$$F(\theta) = \begin{cases} \cos[0.93(\theta + 7)], & \theta \geq -7.0 \\ \cos[1.12(\theta + 7)], & \theta \leq -7.0 \end{cases}. \quad (14)$$

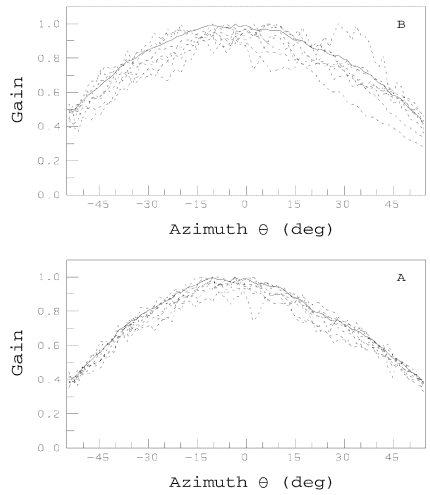


Fig. 1. Individual (broken lines) and average (solid) element gain patterns before (B) and after (A) calibration.

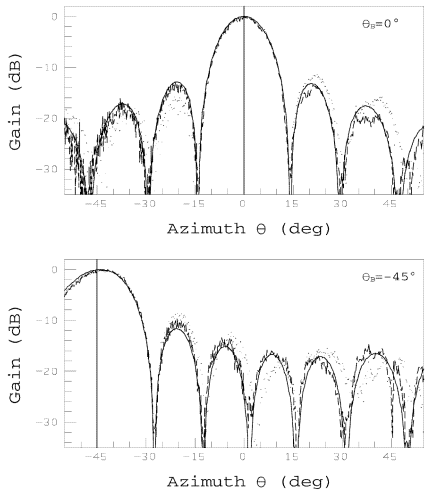


Fig. 2. Ideal (solid lines), measured (dotted), and calibrated (broken) array beam patterns for beam steering directions $\theta_B = 0°$ and $\theta_B = -45°$. The vertical lines are drawn through $\theta_B$.

## B. Array Beam Patterns

The calibrated beam pattern should be close to the ideal pattern for all beam steering directions. In the mainlobe and sidelobe regions, its deviation from the ideal pattern should also be smaller than that of the measured pattern.

The ideal, measured, and calibrated beam patterns had been calculated with the snapshots in File 3 as

$$B_{\text{idl}}(\theta_B,\theta_m) = \beta_{\text{idl}} F(\theta_m)|\mathbf{a}_B^{\text{H}}\mathbf{a}_m|^2 \tag{15a}$$

$$B_{\text{mea}}(\theta_B,\theta_m) = \beta_{\text{mea}}|\mathbf{a}_B^{\text{H}}\mathbf{y}_m|^2 \tag{15b}$$

$$B_{\text{cal}}(\theta_B,\theta_m) = \beta_{\text{cal}}|\mathbf{a}_B^{\text{H}}\mathbf{y}_m^c|^2 \tag{15c}$$

respectively. Angle $\theta_B$ was the beam steering direction and was the direction of a snapshot in the file; $\beta_{\text{idl}}$, $\beta_{\text{mea}}$, and $\beta_{\text{cal}}$ were real scalars used to make the pattern values equal to unity for $\theta_m = \theta_B$; and $\mathbf{a}_B$ and $\mathbf{a}_m$ were array steering vectors for azimuth directions $\theta_B$ and $\theta_m$, respectively. Vector $\mathbf{a}_m$, for example, was calculated as

$$\mathbf{a}_m = (1, \exp[j\delta_m], \ldots, \exp[j(N-1)\delta_m])^{\text{T}} \tag{16}$$

with $\delta_m = 2\pi d \sin\theta_m$, and $d = 0.508$ = element spacing in wavelengths.

The upper half of Fig. 2, calculated with File 3, contains the ideal (solid line), measured (dotted) and calibrated (dashed) beam patterns for $\theta_B = 0°$, a direction where one normally expects to see the best match between the ideal and calibrated patterns. A vertical line through $\theta_B = 0°$ has been added to study the shifts in the mainlobes. In the figure, the peaks of the mainlobes are shifted slightly toward the $-7.0°$ peak position of $F(\theta)$; the measured pattern deviates noticeably from the ideal pattern in the sidelobe regions; and the deviation is smaller for the calibrated pattern.

The lower half of Fig. 2 shows the patterns for $\theta_B = -45°$, a direction close to the lower limit of azimuth directions in File 3. Here, all mainlobes are shifted several degrees toward $-7.0°$. The calibrated pattern is closer to the ideal pattern for $\theta < 40°$.

## C. Relative Powers and Errors in Relative Phases

Ideally, the powers in the components of each $\mathbf{y}_m$ are equal and the relative phases in these components are the same as those of $\mathbf{a}_m$. Deviations from ideal values could be caused by many sources such as the presence of noise, an error in the value of $\theta_m$, and calibration error.

The relative powers in $\mathbf{y}_m$ were calculated as $10 * \log_{10}(|y_{nm}|^2)$ dB minus the average $10 * \log_{10}(|\mathbf{y}_m|^2/N)$; and the error in relative phase for the $n$th element, denoted by $\text{Err}(\phi_{nm})$, was identified as angle $(y_{nm}/a_{nm})$ minus the average for $n = 1$ to $N$. Figs. 3 and 4 show the results obtained by using every 20th snapshot in File 3. Before calibration (B), the average deviation of relative powers from the ideal value of 0 dB is 0.65 dB and the average magnitude of errors in relative phase is 7.4°. After calibration (A), they are 0.43 dB and 2.6°, respectively.

## D. Alignment of Snapshots with Array Steering Vectors

Any single-target array snapshot has the decomposition

$$\mathbf{y} = \alpha\mathbf{a} + \alpha\mathbf{b} + \mathbf{e} \tag{17}$$

where $\mathbf{b}$ originates from errors in calibration and $\mathbf{e}$ is the sum of interference and noise. In the special case of a snapshot given by (2), $\mathbf{b} = \mathbf{b}_m = \mathbf{B}\mathbf{a}_m - \mathbf{a}_m$.

In (17), the true interference plus noise is $\mathbf{e}$; the effective interference plus noise is $\alpha\mathbf{b} + \mathbf{e}$; the component of $\mathbf{y}$ parallel to $\mathbf{a}$ is given by

$$\mathbf{y}_{\|} = \alpha\mathbf{a} + \alpha\mathbf{b}_{\|} + \mathbf{e}_{\|} \tag{18}$$

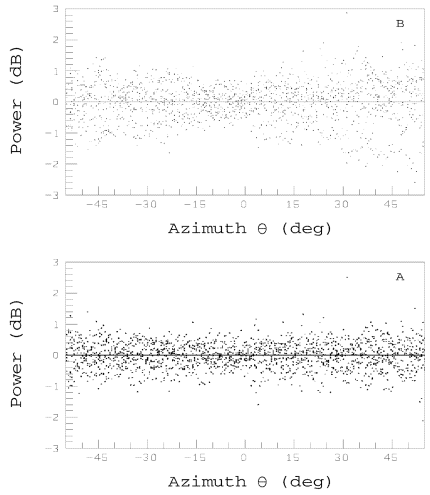


Fig. 3. Relative powers at array elements in snapshots of File 3 before (B) and after (A) calibration.

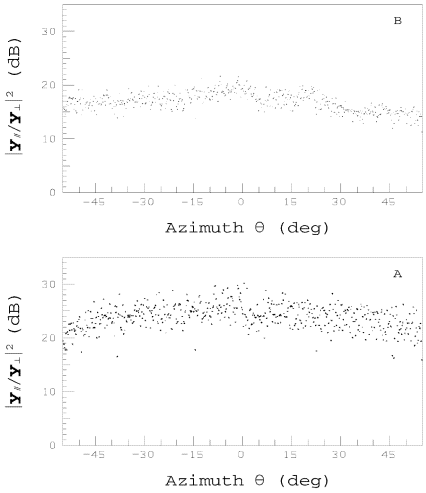


Fig. 5. Values of $|\mathbf{y}_\parallel/\mathbf{y}_\perp|^2$ (dots) before (B) and after calibration (A).

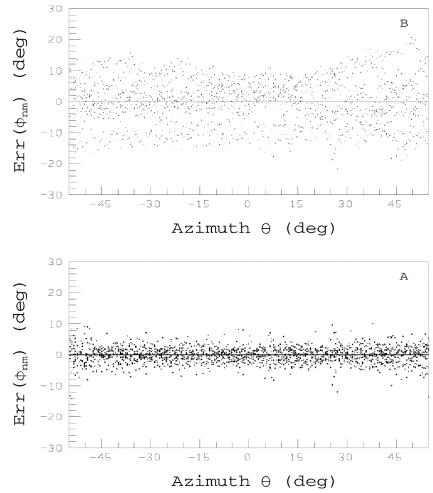


Fig. 4. Errors in relative phases at array elements in the snapshots of File 3 before (B) and after (A) calibration.

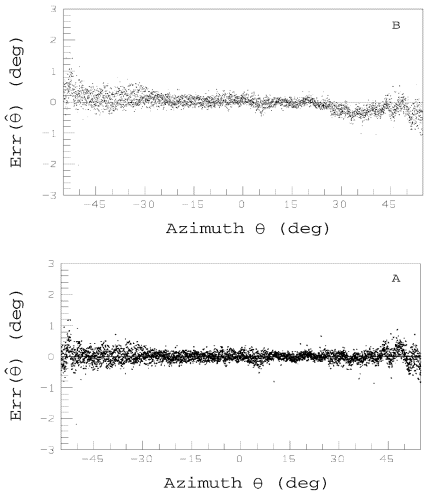


Fig. 6. Errors in source azimuth estimates before (B) and after (A) calibration.

where, for example, $\mathbf{b}_\parallel = (\mathbf{a}^H\mathbf{b})\mathbf{a}/|\mathbf{a}|^2$; and the component orthogonal to $\mathbf{a}$ is

$$\mathbf{y}_\perp = \alpha(\mathbf{b} - \mathbf{b}_\parallel) + (\mathbf{e} - \mathbf{e}_\parallel). \tag{19}$$

The ratio $|\mathbf{y}_\parallel/\mathbf{y}_\perp|^2$ measures how well $\mathbf{y}$ is aligned with $\mathbf{a}$. A larger value means a better alignment and an infinite value means perfect alignment. In Fig. 5 are the ratios (dots) calculated with File 3. Before calibration (B), most values are between 13 and 20 dB. After calibration (A), they are between 20 and 28 dB. Most increases due to calibration are between 7 and 10 dB.

## E. Errors in Direction Estimates

The TKSVD method [3, 4] was used to calculate $L_F$ candidate direction estimates from each snapshot in File 3, assuming that $N_T$ targets were present. The $N_T$ candidate direction estimates with the largest powers were identified as the target direction estimate. Given that $\hat{\theta}_m$ was the estimate of $\theta_m$, the error in $\hat{\theta}_m$ was calculated as

$$\text{Err}(\hat{\theta}_m) = \hat{\theta}_m - \theta_m. \tag{20}$$

In Fig. 6 are the errors (dots) calculated with $L_F = 5$ and $N_T = 1$. These values of $L_F$ and $N_T$ were chosen because they produced errors with the smallest mean square value before calibration. The upper half of the figure shows that, before calibration (B), the errors have a linear component that decreases from 0.4° at $\theta = -55°$ to $-0.5°$ at $\theta = 55°$. They also have an oscillating component that is very visible for $\theta > 40°$. The scattering of errors about the linear component is generally larger if $|\theta|$ is larger. It is also different for $\theta < 0$ and $\theta > 0$. After calibration (A), the linear component is not visible and the average magnitude of the scattering is slightly reduced.

The linear component could originate from a combination of errors in array orientation and

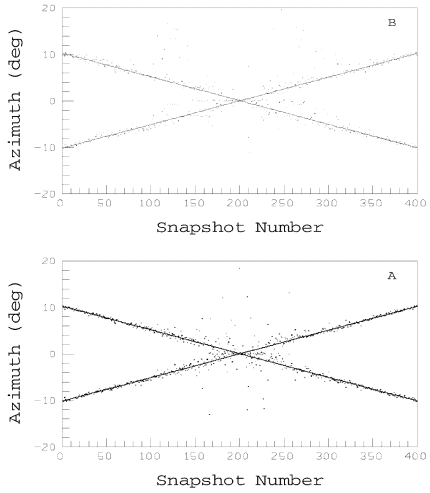


Fig. 7. Target azimuth estimates (dots) before (B) and after (A) calibration. The true target tracks (solid lines) intersect at 0°.

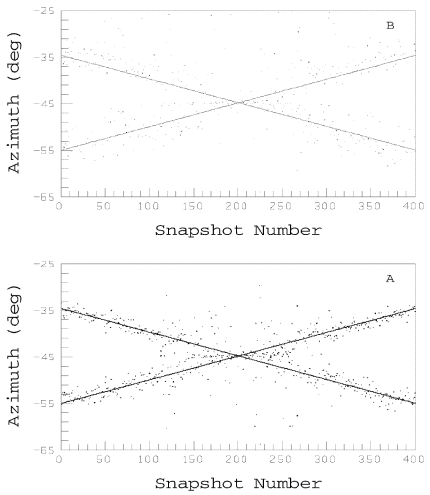


Fig. 8. Target azimuth estimates (dots) before (B) and after (A) calibration. The true target tracks (solid lines) intersect at −45°.

angular speed of the rotating platform. The oscillating component comes from platform vibration, which seemed to increase with $|\theta|$. The scattering is caused by platform vibration and noise. This scattering is generally larger if $|\theta|$ is larger, because the element gain is lower.

## F. Direction Estimates from Two-Target Snapshots

A section of $2K$ snapshots $\{\mathbf{y}'_1,\mathbf{y}'_2,\ldots,\mathbf{y}'_{2K}\}$, with source directions $\{\theta'_1,\theta'_2,\ldots,\theta'_{2K}\}$, was extracted from File 1 and used to construct a synthetic file $\{\mathbf{z}_1,\mathbf{z}_2,\ldots,\mathbf{z}_K\}$ with two uncorrelated targets present as

$$\mathbf{z}_k = \mathbf{y}'_{2k-1} + \exp[j\phi_k]\mathbf{y}'_{2K-2k+2}, \qquad k = 1,2,\ldots,K \tag{21}$$

where $\phi_k$ was a random phase. The TKSVD method was then used to estimate the target directions from each $\mathbf{z}_k$, using $L_F = 5$ and $N_T = 2$.

One target in the synthetic file was in the set of $K$ snapshots $\{\mathbf{y}'_1,\mathbf{y}'_3,\ldots,\mathbf{y}'_{2K-1}\}$, where its direction changed from $\theta'_1$ to $\theta'_{2K-1}$. The other was in $\{\mathbf{y}'_{2K},\mathbf{y}'_{2K-2},\ldots,\mathbf{y}'_2\}$, where the direction changed from $\theta'_{2K}$ to $\theta'_2$. These two targets intersected near $\theta'_K$.

Fig. 7 shows the results obtained with a section of $2K = 800$ snapshots centred at 0° azimuth in File 1. The snapshot number refers to the subscript of $\mathbf{z}_k$. There are two target tracks (solid lines). One track direction increases from −10° to 10° azimuth and the other decreases from 10° to −10°. After calibration (B), the estimates are closer to the solid lines. There is also a better resolution of target directions near the track intersection. Fig. 8 shows the results obtained with a $2K = 800$ section centred at −45° azimuth. There are similar improvements after calibration.

## G. Probability of Resolving two Equistrength Targets

A section of $K$ snapshots from File 1 was used to construct $K(K-1)/2$ synthetic snapshots with two uncorrelated equistrength targets present as

$$\mathbf{z}_{p,q} = \mathbf{y}'_p + \exp[j\phi_{p,q}]\mathbf{y}'_q \qquad p > q, \quad p,q = 1,2,\ldots,K. \tag{22}$$

Here, $\mathbf{y}'_p = \mathbf{y}_p/|\mathbf{y}_p|$, $\mathbf{y}'_q = \mathbf{y}_q/|\mathbf{y}_q|$ and $\phi_{p,q}$ was a random phase. The TKSVD method was then used to calculate two target direction estimates, denoted by $\{\hat{\theta}_{z,1},\hat{\theta}_{z,2}\}$, from each $\mathbf{z}_{p,q}$, using $L_F = 5$ and $N_T = 2$. The targets were then considered resolved if

$$|\hat{\theta}_{z,1} - \hat{\theta}_p| \qquad \text{and} \qquad |\hat{\theta}_{z,2} - \hat{\theta}_q| < 0.5|\hat{\theta}_p - \hat{\theta}_q| \tag{23a}$$

or

$$|\hat{\theta}_{z,1} - \hat{\theta}_q| \qquad \text{and} \qquad |\hat{\theta}_{z,2} - \hat{\theta}_p| < 0.5|\hat{\theta}_p - \hat{\theta}_q|. \tag{23b}$$

Angles $\hat{\theta}_p$ and $\hat{\theta}_q$ were single-target direction estimates calculated with $\mathbf{y}_p$ and $\mathbf{y}_q$, respectively. Nominal values $\theta_p$ and $\theta_q$ were not used, because they had errors due to platform vibration.

The upper half of Fig. 9 shows the probabilities of resolving two targets close to 0° azimuth before (dotted curve) and after (solid) calibration. It was generated with the same 800 snapshots used in Fig. 7. They are plotted as functions of $Nd|\sin\hat{\theta}_p - \sin\hat{\theta}_q|$, which is approximately equal to the target separation in beamwidths. Evidently, the calibration increased the probability of target resolution. This increase was approximately 0.28 for angular separations close to 0.3 beamwidth.

The lower half of Fig. 9 shows the probabilities of resolving two targets close to −45° azimuth and was generated with the data used in Fig. 8. The calibration also increased the resolution probability

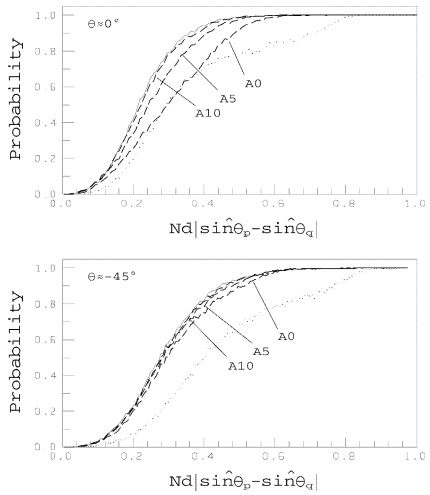


Fig. 9. Probability of resolving two equistrength targets before (dotted curve) and after (solid) calibration for target directions close to 0° and −45°. In dashed curves A10, A5, and A0, an unknown interference was present in the calibration data and the SIRs were 10, 5, and 0 dB, respectively.

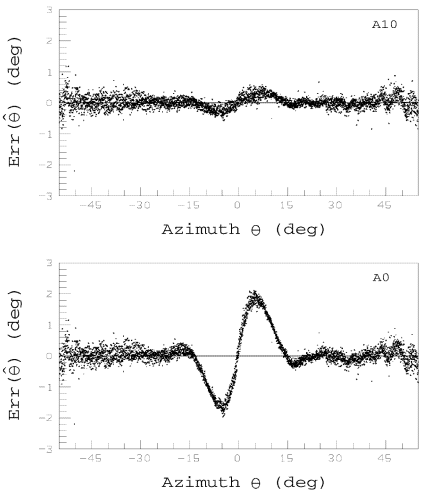


Fig. 10. Errors in source azimuth estimates after calibration. An unknown interference was present in the calibration data. The SIRs were 10 dB in the upper half (A10) and 0 dB in the lower (A0).

TABLE III
Values of $\max\{|D_{pq}|\}$ and $\text{std}\{|D_{pq}|\}$ in $\mathbf{D}'$ and $\mathbf{D}''$

| | $\mathbf{D}''$ | | | $\mathbf{D}'$ |
|---|---|---|---|---|
| SIR (dB) | 0 | 5 | 10 | / |
| $\max\{\lvert D_{pq}\rvert\}$ | 0.062 | 0.035 | 0.019 | 0.013 |
| $\text{std}\{\lvert D_{pq}\rvert\}$ | 0.045 | 0.023 | 0.011 | 0.004 |

and the increase was approximately 0.33 for angular separations between 0.3 and 0.5 beamwidths.

## H. Dependence of C on Calibration Data

Different sets of calibration data should produce essentially the same calibration matrix, if each set satisfies all the measurement conditions of the calibration method.

File 3 also satisfied all the measurement conditions of the calibration method. It was used to calculate a new matrix $\mathbf{C}'$ and the difference $\mathbf{D}' = \mathbf{C}' - \mathbf{C}$. Column 5 of Table III gives the largest magnitude, $\max\{|D'_{pq}|\}$, and the standard deviation of the magnitudes, $\text{std}\{|D'_{pq}|\}$, of the coefficients in $\mathbf{D}'$. They are 0.013 and 0.004, respectively. Because $C'_{11} = C_{11} = 1.0$, one can conclude that $\mathbf{C}'$ and $\mathbf{C}$ are essentially the same and that Files 2 and 3 produced essentially the same calibration matrix.

## I. Tolerance to Unknown Interference

Tolerance to unknown interference is essential if an antenna array can only be calibrated in-situ and interference cannot be ignored. The reason for in-situ calibration could be heavy antenna weight, large physical size, or unacceptable changes in antenna characteristics introduced by the disassembly-transportation-reassembly process.

The tolerance of the calibration method to unknown interference was studied by the injection of an interference with azimuth $\theta_I$ close to 0°. Initially, the interference was added to each snapshot in File 2 as

$$\mathbf{y}''_m = \mathbf{y}_m + \rho \exp[j\phi_m]\mathbf{y}_I, \qquad m = 1,2,\ldots,M \tag{24}$$

where $\rho$ was a parameter used to make the average of $|\mathbf{y}_m/\rho\mathbf{y}_I|^2$ equal to a specified signal to interference ratio (SIR), $\phi_m$ was a random phase, $\mathbf{y}_I$ was a snapshot with the interference direction $\theta_I$, and $M$ was the number of snapshots in the file. Next, the modified File 2 was used to calculate a calibration matrix $\mathbf{C}''$. Finally, the visual difference between $\mathbf{C}''$ and $\mathbf{C}$, the coefficients in the difference $\mathbf{D}'' = \mathbf{C}'' - \mathbf{C}$, and the effect of using $\mathbf{C}''$ instead of $\mathbf{C}$ to calibrate File 3 were examined. Some notable results are given below.

1) Matrix $\mathbf{C}''$ did not look very different from $\mathbf{C}$, if SIR > 0 dB. Some examples are given in Columns 2, 3, and 4 of Table III, which contain the values of $\max\{|D''_{pq}|\}$ and $\text{std}\{|D''_{pq}|\}$ for SIR = 0, 5, and 10 dB, respectively. With SIR = 10 dB, the values are close to those of $\mathbf{D}'$ in column 5. With SIR = 0 dB, they are 0.062 and 0.045, respectively. These values are not large enough to make $\mathbf{C}''$ look very different from $\mathbf{C}$.

2) The errors in direction estimates, given by $\hat{\theta}_m - \theta_m$, had the properties shown in Fig. 10. In this figure, the effect of the interference is negligible outside the region $-15° < \theta_m < 15°$. Inside this region, the error has the same sign as $\theta_m - \theta_I$; the largest error magnitudes are approximately 0.5° for SIR = 10 dB and 2° for SIR = 0 dB. Errors 0.5° and 2.0° are approximately equal to 0.04 and 0.16 beamwidths,

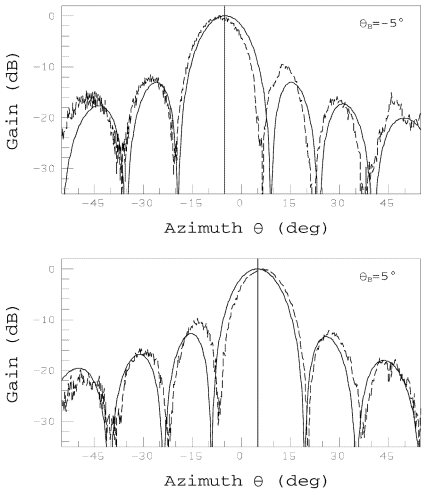


Fig. 11. Ideal (solid line) and calibrated (broken) array beam patterns for beam steering direction $\theta_B = -5°$ and 5°. The SIR in the calibration data was 0 dB and the vertical lines are drawn through $\theta_B$.

respectively, because the antenna array aperture is approximately four wavelengths and one beamwidth in the interference direction is approximately 12.5°.

3) The interference usually shifted the peaks of the mainlobes and simultaneously distorted the sidelobes in the array beam patterns. If $\theta'_B$ was the shifted peak position, the shift $\theta'_B - \theta_B$ had the same sign as $\theta_B - \theta_I$. An illustration is given in Fig. 11, which contains the patterns calculated with $\theta_B = -5°$ and 5°. In the $\theta_B = -5°$ pattern, where $\theta_B - \theta_I \approx -5°$, one has $\theta'_B - \theta_B \approx -2°$. Similarly, in the $\theta_B = 5°$ pattern, $\theta_B - \theta_I \approx 5°$ and $\theta'_B - \theta_B \approx 2°$.

4) The interference reduced the probability of resolving two targets. This reduction was smaller if a) the SIR was larger, or b) the target direction was farther away from the interference direction $\theta_I$. Dashed curves A10, A5, and A0 in Fig. 9 are examples of this property. They were calculated with $\mathbf{C}''$ instead of $\mathbf{C}$ and the set of $\{\mathbf{z}_{p,q}\}$ used to produce curves A and B. The SIRs were 10, 5, and 0 dB, respectively. In the top half, where the target directions were close to the interference direction $\theta_I$, curves A10 and A5 are above curve B and A0 is slightly below B for $Nd|\sin\hat{\theta}_p - \sin\hat{\theta}_q|$ between 0.30 and 0.41. Compared with the interference-absent probabilities in curve A, the largest reduction is less than 0.03 for SIR = 10 dB and less than 0.15 for SIR = 5 dB. The bottom half of Fig. 9 gives the resolution probabilities for target directions close to −45°. Curves A10, A5, and A0 are above curve B. The reductions are less than 0.06 for the three values of SIR.

The case of an interference with SIR = 0 dB corresponded to an extremely unlikely situation in which the interference was just as strong as the pilot signal and was not observed. From the above results, this interference only marginally degraded the performance of the array for signal directions more than 15°, or 1.2 beamwidths, from $\theta_I$. For other directions, the degradation was acceptable, because the largest error in direction estimate was approximately 0.16 beamwidth and the resolution probabilities, given by curve A0 in the upper half of Fig. 9, were generally higher than those in curve B.

## V. CONCLUSIONS

This paper gave a brief description of the antenna array calibration method in [1]. It then evaluated the method with experimental data. The results showed that the method 1) reduced the deviation of element gain patterns from the true pattern, the deviation of array beam patterns from the ideal pattern, the deviation of relative element output powers from 0 dB, the deviation of errors in the relative phases from 0°, the errors in single-target and two-target direction estimates calculated with the TKSVD method; 2) increased the alignment of single-target array snapshots with the array steering vectors and the probability of resolving two targets as their angular separation decreased to zero; 3) produced essentially the same calibration matrix with a different set of calibration data; 4) was highly tolerant to the presence of unknown interference.

The evaluation technique in this paper can be used to compare different antenna array calibration methods. It can distinguish methods that improve the array performances for all signal directions from those that optimize the performances for some configurations only. It can also distinguish methods that can calibrate arrays under harsh interference conditions from those that require controlled environments.

The calibration method in [1] has been modified to calibrate a maritime low-angle tracking antenna array in the presence of specular multipath reflections from the water surface. This work will be presented in a separate paper.

## ACKNOWLEDGMENT

This author would like to thank Bob Hicks, Jay Loomis, and John Rose of the U.S. Army Missile Command, Redstone Arsenal, Alabama for supplying the experimental data under the auspices of the The Technical Cooperation Program.

## REFERENCES

[1] Hung, E. K. L. (1994)
Computation of the coupling matrix among the elements of an array antenna.
In *Proceedings of the International Conference on Radar* (Radar 94), Paris, May 1994, 703–706.

[2] Schmidt, R. O. (1986)
Multiple emitter location and signal parameter estimation.
*IEEE Transactions on Antennas and Progagation*, **AP-34** (Mar. 1986), 276–280.

[3] Tufts, D. W., and Kumarisen, R. (1982)
Estimation of frequencies of multiple sinusoids: Making linear prediction perform like maximum likelihood.
*Proceedings of the IEEE*, **70** (Sept. 1982), 975–989.

[4] Tufts, D. W., and Kumarisen, R. (1983)
Estimating the angle of arrival of multiple plane waves.
*IEEE Transactions on Aerospace and Electronic Systems*, **AES-19** (Jan. 1983), 134–139.

[5] Friedlander, B. (1990)
A sensitivity analysis of the MUSIC algorithm.
*IEEE Transactions on Acoustics, Speech, and Signal Processing*, **38** (Oct. 1990), 1740–1751.

[6] Friedlander, B. (1990)
Sensitivity analysis of the maximum likelihood direction-finding algorithm.
*IEEE Transactions on Aerospace and Electronic Systems*, **26** (Nov. 1990), 953–968.

[7] Swindlehurst, A., and Kailath, T. (1992)
A performance analysis of subspace-based methods in the presence of model errors—Part I: The MUSIC algorithm.
*IEEE Transactions on Signal Processing*, **40** (July 1992), 1758–1774.

[8] Swindlehurst, A., and Kailath, T. (1993)
A performance analysis of subspace-based methods in the presence of model errors—Part II: Multidimensional algorithms.
*IEEE Transactions on Signal Processing*, **41** (Sept. 1993), 1277–1308.

[9] Li, F., and Vaccaro, R. J. (1992)
Sensitivity analysis of DOA estimation algorithms to sensor errors.
*IEEE Transactions on Aerospace and Electronic Systems*, **28** (July 1992), 708–717.

[10] Weiss, A. J., and Friedlander, B. (1988)
Direction-finding in the presence of mutual coupling.
In *Conference Record of the 22nd Asilomar Conference on Signals, Systems and Computers*, Pacific Grove, CA, Nov. 1988.

[11] Pierre, J., and Kaveh, M. (1991)
Experimental performance of calibration and direction-finding algorithms.
In *Proceedings of the International Conference on Acoustics, Speech, and Signal Processing*, ICASSP 91, Toronto, Canada, May 1991, 1365–1368.

[12] See, C. M. S. (1994)
Sensor array calibration in the presence of mutual coupling and unknown gains and phases.
*Electronics Letters*, **30**, 5 (Mar. 1994), 373–374.

[13] Hung, E. K. L. (1994)
A critical study of a self-calibrating direction-finding method for arrays.
*IEEE Transactions on Signal Processing*, **42**, 2 (Feb. 1994), 471–474.

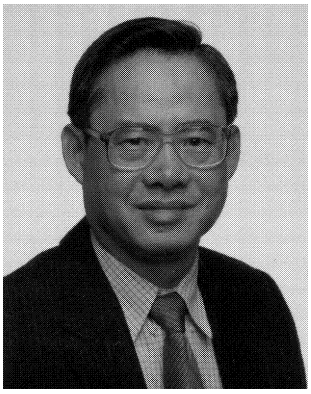

**Eric Kam-Ling Hung** was born in Hong Kong in 1938. He received a B.Sc. General Honours degree in 1962 and a B.Sc. Special Honours degree in 1964 from the University of Hong Kong, an M.Sc. degree in physics from the University of Manitoba in 1965, a Ph.D. degree in physics from the University of Alberta in 1970, and an M.Eng. degree in electrical engineering from Carleton University, Ottawa, in 1976.

He was a teacher in Hong Kong from 1962 to 1964, an engineer at Computing Devices Company in Ottawa from 1970 to 1977, a research scientist at the Communications Research Centre in Ottawa from 1977 to 1986. Since 1986, he has been working as a defence scientist at the Defence Research Establishment Ottawa, Canada. His experience includes high school teaching, submarine detection, and radar research. At present, he is working in the development of a high frequency surface wave radar for coastal surveillance.